Low-loss low thermo-optic coefficient Ta$_2$O$_5$ on crystal quartz planar optical waveguides

EP

Qiancheng Zhao, Ryan O. Behunin, Peter T. Rakich, Nitesh Chauhan, Andrei Isichenko, Jiawei Wang, Chad Hoyt, Chad Fertig, Mu hong Lin, and Daniel J. Blumenthal

COLLECTIONS

EP   This paper was selected as an Editor's Pick

View Online   Export Citation   CrossMark

ARTICLES YOU MAY BE INTERESTED IN

Silicon nitride chirped spiral Bragg grating with large group delay
APL Photonics **5**, 101302 (2020); https://doi.org/10.1063/5.0022963

Tubular optical microcavities based on rolled-up photonic crystals
APL Photonics **5**, 106106 (2020); https://doi.org/10.1063/5.0022862

Photonic integration for UV to IR applications
APL Photonics **5**, 020903 (2020); https://doi.org/10.1063/1.5131683

Low-loss low thermo-optic coefficient Ta$_2$O$_5$ on crystal quartz planar optical waveguides 🔵ᴱᴾ

Qiancheng Zhao,[1] 🔵 Ryan O. Behunin,[2,3] Peter T. Rakich,[4] Nitesh Chauhan,[1] Andrei Isichenko,[1] Jiawei Wang,[1] Chad Hoyt,[5] Chad Fertig,[5] Mu hong Lin,[5] and Daniel J. Blumenthal[1,a] 🔵

AFFILIATIONS

[1] Department of Electrical and Computer Engineering, University of California, Santa Barbara, Santa Barbara, California 93106, USA
[2] Department of Applied Physics and Material Sciences, Northern Arizona University, Flagstaff, Arizona 86011, USA
[3] Center for Materials Interfaces in Research and Applications (¡MIRA!), Northern Arizona University, Flagstaff, Arizona 86011, USA
[4] Department of Applied Physics, Yale University, New Haven, Connecticut 06511, USA
[5] Honeywell Aerospace, Plymouth, Minnesota 55441, USA

[a] Author to whom correspondence should be addressed: danb@ucsb.edu

ABSTRACT

Optical resonator-based frequency stabilization plays a critical role in ultra-low linewidth laser emission and precision sensing, atom clocks, and quantum applications. However, there has been limited success in translating traditional bench-top stabilization cavities to compact on-chip integrated waveguide structures that are compatible with photonic integration. The challenge lies in realizing waveguides that not only deliver low optical loss but also exhibit a low thermo-optic coefficient and frequency noise stability. Given the problematic sources of frequency noise within dielectrics, such as thermorefractive noise, resonators with small thermo-optic response are desirable for on-chip reference cavities. We report the first demonstration of a Ta$_2$O$_5$ (tantala) waveguide core fabricated on a crystal quartz substrate lower cladding with TEOS-PECVD SiO$_2$ upper cladding. This waveguide offers significant advantages over other waveguides in terms of its low thermo-optic coefficient and reduced thermorefractive-related frequency noise. We describe the waveguide structure and key design parameters as well as fabrication considerations for processing tantala on quartz waveguides. We report a waveguide thermo-optic coefficient of -1.14×10^{-6} RIU/K, a value that is over 6 times smaller in magnitude than that of SiO$_2$-substrate tantala waveguides, with a propagation loss of 1.19 dB/cm at 1550 nm and <1.33 dB/cm across the 1525 nm–1610 nm wavelength range. Within a 1.6 mm radius ring resonator, we demonstrate a 2.54×10^5 intrinsic Q factor. With the potential for very low loss and the ability to control the thermal response, this waveguide platform takes a key step toward creating thermally stable integrated resonators for on-chip laser frequency stabilization and other applications.

I. INTRODUCTION

Optical reference cavities are used for frequency stabilization and linewidth narrowing in precision high-end applications in physics such as precision spectroscopy,[1] metrology,[2,3] and atomic clocks.[4,5] By harnessing ultra-high quality factors (Qs), large mode volumes, and low thermal sensitivity, reference cavities deliver a stable frequency resonance and low close-to-carrier noises, i.e., frequency noise spectral density close to the optical carrier. State-of-the-art table-top reference cavities consist of a Fabry–Perot resonator made of ultra-low-expansion glass (ULE)[6] or a single crystal silicon cavity mounted in an isolated vacuum cryogenic environment.[7] For lower cost and portable applications, it is desirable to miniaturize these cavities using photonic integration waveguide-based designs.[8] However, integrated optical resonators suffer more severely from the thermodynamic fluctuations[9] due to their small mode volumes and nontrivial thermal sensitivities caused by thermorefractive and thermal expansion effects. While thermal expansion can be controlled by attaching resonators to substrates with zero or negative thermal expansion coefficients,[10,11] thermorefractive

effects still produce undesired frequency instability within dielectric resonators.

The thermorefractive frequency noise of an integrated reference cavity is directly tied to the waveguide thermo-optic coefficient[12] as well as the optical mode volume.[13–15] Through proper waveguide material choice and design, the effective thermo-optic coefficient (TOC_{eff}) and mode volume can be optimized to reduce the thermorefractive frequency noise components.[16] For this purpose, crystal quartz has attractive optical and thermal properties such as a wide transparency window (0.2 μm–2 μm), optical birefringence, and a negative thermo-optic coefficient, e.g., -7.94×10^{-6} RIU/K (RIU: refractive index unit) at 1550 nm for ordinary waves.[17] Bulk-optic quartz has been used to fabricate high performance whispering-gallery-mode resonators,[18,19] but these systems are environmentally sensitive, costly to fabricate and package, and are incompatible with photonic integration. In the past, efforts to realize quartz-based integrated waveguides[20–23] resulted in propagation loss as high as 10 dB/cm,[20,22] and they could not support the waveguide bends required for waveguide ring resonators. In addition, the negative TOC property of quartz has not been demonstrated in a composite integrated waveguide. As a result, the realization of low-loss integrated waveguides on quartz substrates will enable novel photonic devices with extraordinary thermo-optic properties, opening new possibilities for photonic integrated reference cavities.

In this work, we report the first demonstration of Ta_2O_5 (tantala) core strip waveguides on a crystal quartz substrate with SiO_2 upper cladding. We measure a low propagation loss of 1.19 dB/cm at 1550 nm wavelength for a 4 μm-wide 125 nm-thick Ta_2O_5-core waveguide. With this waveguide design, we fabricated a 1.6 mm-radius resonator and measured an intrinsic Q factor of 2.54×10^5 and a loaded Q factor of 1.95×10^5. In addition, we show that the waveguide effective thermo-optic coefficient is -1.14×10^{-6} RIU/K, six times smaller than a comparison waveguide that has thermal oxide as substrate. The small and negative thermo-optic coefficient demonstrates that using crystal quartz as a waveguide substrate can enable the control of the waveguide thermo-optic coefficient with the potential to suppress thermorefractive frequency noise. Combined with other techniques[10,11] to suppress the thermal expansion, this technology promises a new approach to low thermorefractive noise and low-loss waveguide optical reference cavities for frequency precision applications such as low-energy data center interconnects[24] and ultra-narrow-linewidth on-chip stimulated Brillouin lasers.[25]

II. DEVICE DESIGN AND FABRICATION

The waveguide design and conceptual figure of a spiral waveguide and a ring resonator are depicted in Fig. 1(a). We use a z-cut crystal quartz substrate (with c-axis normal to the surface) to ensure that the refractive index is independent of the waveguide direction. A tantala strip core is deposited and etched on a crystal quartz substrate and cladded with a TEOS-PECVD SiO_2 upper cladding, as described in the Sec. VI. This process is compatible
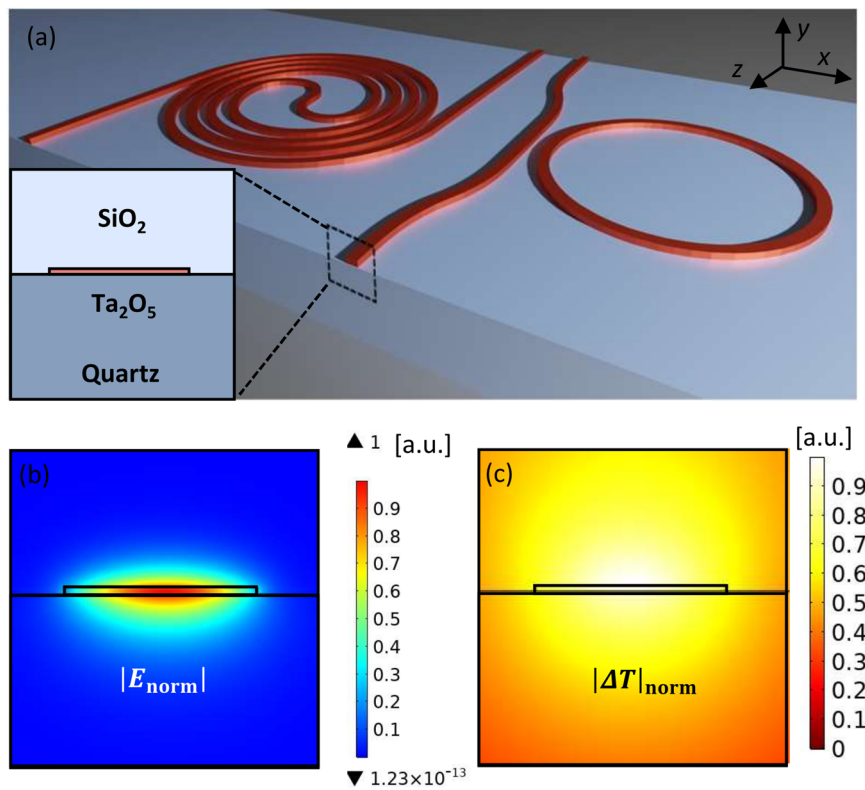

FIG. 1. (a) Conceptual illustration of fabricated waveguide-based structures including an Archimedean spiral delay line and a ring resonator. The upper cladding is artificially transparent to reveal the details of the waveguide core. A cross section of the waveguide and its constituent materials are shown in the inset. (b) The normalized electric–field profile of the fundamental TE mode in the waveguide. (c) The normalized temperature variation induced by material absorption of the optical power. The normalized temperature variation is defined as $|\Delta T|_{norm} = (T(x, y) - T_{min})/(T_{max} - T_{min})$.

with wafer-scale low-temperature fabrication. We employ a high-aspect-ratio weakly guiding waveguide geometry similar to those used in ultra-low loss silicon nitride[26] and tantala on oxide substrate designs,[27] with its fundamental TE mode shown in Fig. 1(b). Material absorption-induced temperature variations [Fig. 1(c)] perturb the optical constants and mechanical expansion, which will translate into frequency noise in resonators when optical power fluctuates. With the objective to suppress the thermorefractive fluctuations, this designed waveguide geometry has a large optical mode overlap with the quartz substrate, yielding a slightly negative but *close-to-zero* TOC_{eff}, which reduces the overall sensitivity of the mode effective index to temperature variations.

The Ta_2O_5-core on crystal quartz waveguides is fabricated in a similar approach as reported in our previous work,[27] except without thermal annealing after Ta_2O_5 film deposition and after TEOS-PECVD SiO_2 upper cladding deposition (see Sec. VI for fabrication details). High temperature thermal annealing was not used in the fabrication process for two reasons: (1) to avoid thermal shock and film peeling caused by the large thermal expansion coefficient mismatch between the crystal quartz substrate (13.2×10^{-6}/K perpendicular to the optical axis[28]) and the deposited films (3.6×10^{-6}/K for

Ta_2O_5.[29] and 0.56×10^{-6}/K for amorphous SiO_2[30]) and (2) because quartz changes from α- to β-phase, with positive thermo-optic coefficient, as the temperature increases beyond 573 °C.[31]

III. WAVEGUIDE PROPAGATION LOSS AND RESONATOR Q FACTORS

The waveguide propagation loss is characterized by using both Q factor measurements in a ring-bus resonator and the optical frequency domain reflectometry (OFDR) method in a waveguide spiral structure. All-pass ring resonators are designed with a radius of 1.6 mm and a 0.5 μm ring-bus waveguide coupling gap. The loaded Q factors of the resonances are measured and verified using two different experiment setups, a RF calibrated Mach–Zehnder interferometer (MZI) setup and a direct laser tuning transmission setup (see Sec. VI for more details). In the former approach, the full width at half maximum (FWHM) of the resonance is $\Delta\nu$ = 991.43 MHz obtained through Lorentzian curve fitting [Fig. 2(b)], giving a loaded Q factor $Q_{load} = \nu_{res}/\Delta\nu = 1.95 \times 10^5$ at 1550 nm, where ν_{res} is the resonant frequency. The power coupling coefficient is measured to
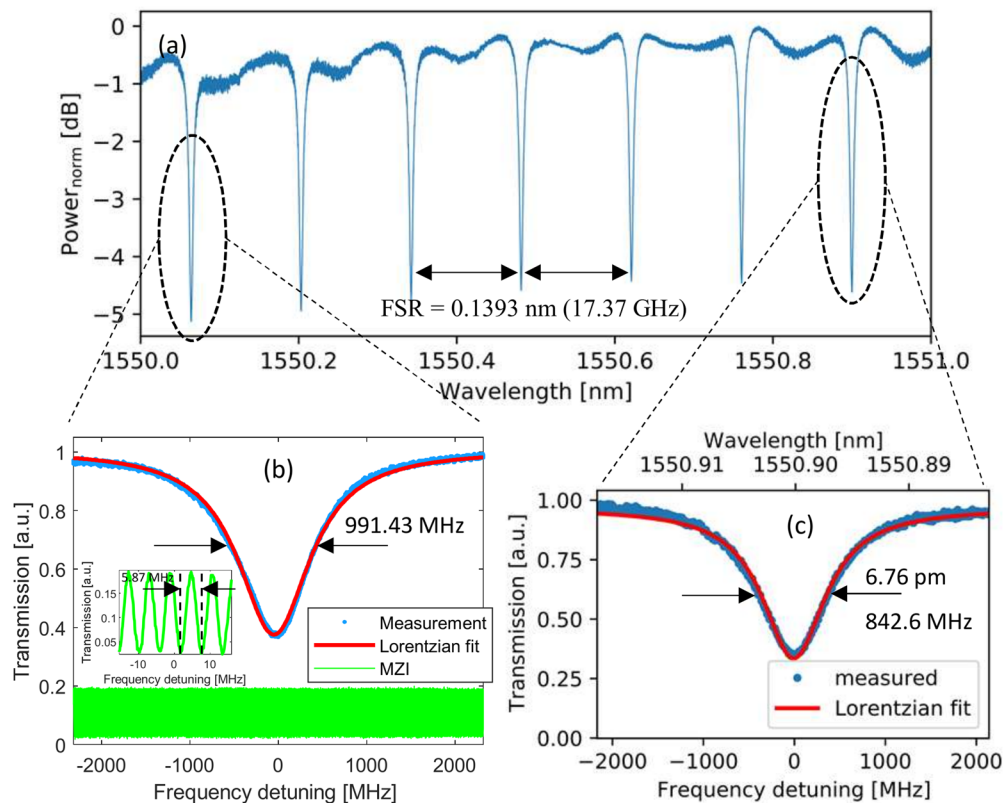

FIG. 2. (a) The transmission spectrum of a 1.6 mm-radius 4 μm-wide all-pass ring resonator in the spectral range from 1550 nm to 1551 nm reveals the TE mode only operation. (b) A zoomed-in figure of one of the resonances in a frequency detuning range of 4.6 GHz. An unbalanced MZI with an FSR of 5.87 MHz is used to calibrate the frequency detuning, and its zoomed-in transmission spectrum is plotted in the inset. The FWHM of the resonance is 991.43 MHz, and the loaded Q is 1.95×10^5. (c) Another zoomed-in figure of one of the resonances around 1550.90 nm. The bottom *x*-axis is converted to frequency detuning to ease the comparison with (b). The wavelength is labeled on the top *x*-axis. The FWHM of the resonance is 842.6 MHz (6.76 pm), and the loaded Q is 2.29×10^5.

be 8% between the ring and the bus waveguides by using the ring-bus coupling test structures on the same die. Correspondingly, the propagation loss of the waveguide is derived to be 1.18 dB/cm and the intrinsic Q factor is estimated to be 2.54×10^5 (see Sec. VI for propagation loss and intrinsic Q factor calculation details). In the second Q factor measurement approach, the input wavelength is precisely controlled by a tunable laser source, and the transmitted power is recorded by a photodetector. Figure 2(a) shows the transmission spectrum of the fundamental TE mode by varying the laser wavelength. The measured free spectral range (FSR) of the resonator is 0.1393 nm, corresponding to 17.37 GHz at 1550 nm. The slight fluctuations of the transmission spectrum are due to the weakly resonant higher order transverse electric mode. The high order TE mode has distinct resonant line shapes (broad resonance and small extinction ratio) from the fundamental TE mode. It has negligible impact on the Lorentzian fitting on the fundamental TE mode resonance and, thus, does not affect the characterization of the fundamental TE mode. The FWHM of one resonance is found to be $\Delta\lambda$ = 6.76 pm (equivalent to 842.6 MHz) through Lorentzian curve fitting [Fig. 2(c)], and the loaded Q factor is $Q_{load} = \lambda_{res}/\Delta\lambda = 2.29 \times 10^5$. Thus, the propagation loss and the intrinsic Q factor are derived to be 0.96 dB/cm and $Q_{inc} = 3.15 \times 10^5$, respectively.

The waveguide propagation loss is also measured by using optical frequency domain reflectometry (OFDR). The tested waveguide is a 4 μm-wide and 0.2 m-long spiral delay line, as shown in Fig. 3(b). The spiral delay line has a minimum bend radius of 800 μm, well above the critical bend radius of 320 μm at which the bending loss is simulated to be 1 dB/m. The measured propagation loss from the OFDR experiment is 1.19 dB/cm at 1550 nm and is lower than 1.33 dB/cm across the 1525 nm–1610 nm spectrum range shown in Fig. 3(a). Waveguide propagation losses measured using OFDR and derived from the MZI-based Q factor measurements agree well with less than 0.9% difference. The experiment details can be found in Sec. VI.

IV. EFFECTIVE THERMO-OPTIC COEFFICIENT

The crystal quartz substrate enables the adjustment of the TOC$_{eff}$ of the optical mode. To obtain the thermo-optic coefficient of the waveguide, we measured the transmission spectrum of the resonator and tracked its resonance at different temperatures

[see Fig. 4(a)], yielding a temperature dependent wavelength shift (TDWS) of 16.3 pm/K. The temperature dependent wavelength shift can be attributed to thermal expansion and thermorefractive effects. Considering a resonance condition of a ring cavity,

$$2\pi R n_{eff} = m\lambda_{res}, \qquad (1)$$

where m is the resonance order. The TOC$_{eff}$ can be derived as

$$\frac{dn_{eff}}{dT} = \frac{n_{eff}}{\lambda_{res}}\frac{d\lambda_{res}}{dT} - \frac{n_{eff}}{R}\frac{dR}{dT}, \qquad (2)$$

where the second term on the right-hand side of Eq. (2), $(1/R)(dR/dT)$, is the effective linear thermal expansion coefficient. To quantify the impact of the thermal expansion and the thermorefractive effects within the waveguide, we use finite-element-method (FEM) models (COMSOL Multiphysics) based on the mechanical, optical, and thermal parameters taken from our measurements as well as values reported in the literature (see the supplementary material for simulation model details). Figure 4(b) shows the simulated resonant wavelengths of a 4 μm-wide resonator caused by the thermal expansion (TE) effect, the thermorefractive (TR) effect, and a combination of both (TE+TR). The measured resonant wavelengths in Fig. 4(a) are also added for comparison, demonstrating a good correlation between the simulation and the experimental results. By comparing the slope of the curve, one can find that thermal expansion is the dominant effect in the total temperature dependent wavelength shift. The thermorefractive curve exhibits a negative slope of −1.139 pm/K from which the TOC$_{eff}$ of the 4 μm-wide waveguide is calculated to be -1.14×10^{-6} RIU/K. To illustrate the validity of the models, we also measure and extract the effective thermo-optic coefficient of a Ta$_2$O$_5$-core thermal oxide-substrate waveguide. The oxide-substrate waveguide has the same waveguide design and fabrication process, except that its substrate is thermal oxide that has a positive thermo-optic coefficient (~9.8 $\times 10^{-6}$ RIU/K[32]). The waveguide loss is measured to be 0.276 dB/cm, and its loaded Q factor is 0.945×10^6 (see the supplementary material). The temperature-dependent transmission spectrum of a 4 μm-wide, 1.6 mm-radius ring resonator is shown in Fig. 4(c). Owing to a larger core/substrate refractive index contrast (~2/1.45 for thermal oxide-substrate waveguides vs ~2/1.53 for crystal quartz-substrate waveguides), a higher order optical mode was observed during the
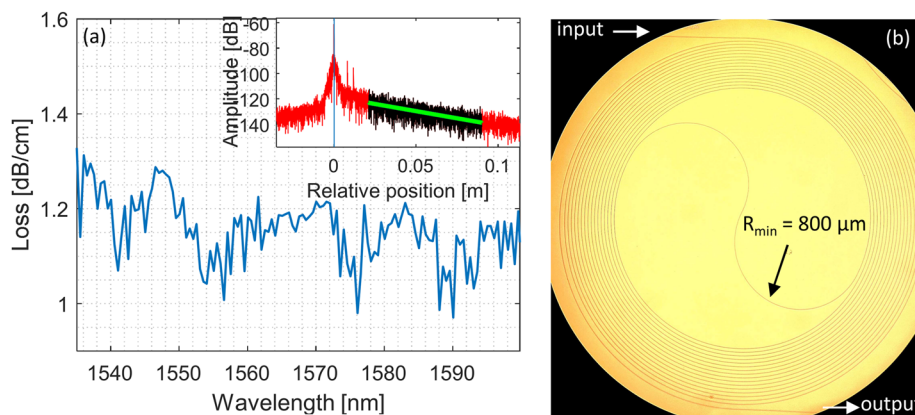
FIG. 3. (a) The waveguide propagation loss spectrum obtained by linear curve fitting from the black region in the inset. The inset shows the overlaid reflected signal amplitudes at different wavelengths as functions of the relative position in a 4 μm-wide optical delay line. The position of the waveguide input facet is set at the origin. The wave propagating direction is set to be positive. The black region indicates where linear curve fitting is performed. The green curve shows the linear fitting curve. (b) The microscope image of a 0.2 m-long spiral delay line with a minimum bend radius of 800 μm.
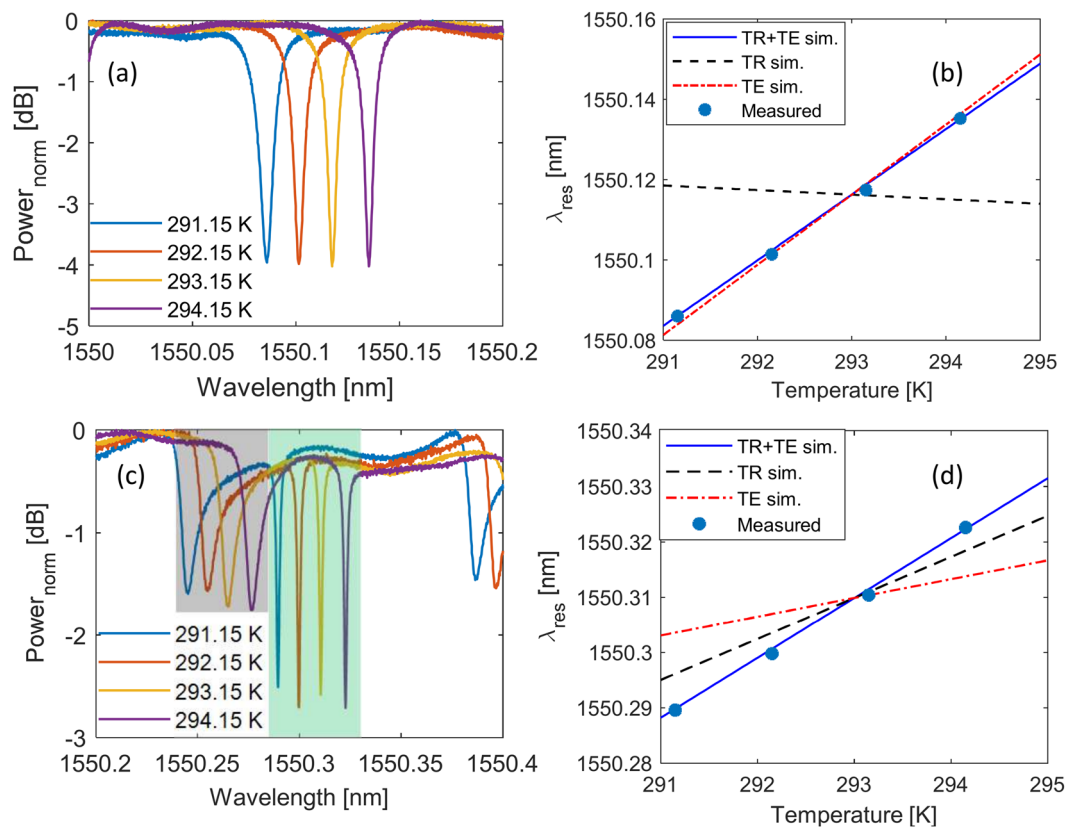
FIG. 4. (a) The temperature-dependent transmission spectrum of a 4 μm-wide Ta_2O_5-core crystal quartz-substrate ring resonator. (b) The simulated and measured resonant wavelengths as a function of temperature. The resonance shifts due to the thermorefractive and the thermal expansion effects are denoted as TR and TE, respectively. (c) The temperature-dependent transmission spectrum of a 4 μm-wide Ta_2O_5-core thermal oxide-substrate ring resonator. The fundamental modes are in the green highlighted region, while higher order modes are in the gray highlighted region. The temperature sensitivity is extracted from the fundamental modes. (d) The simulated and measured resonant wavelengths of the oxide-substrate resonator are plotted as a function of temperature.

measurement with the appearance of second resonance in the transmission spectrum shown in the gray highlighted region in Fig. 4 (c). We measured the resonance shift of the fundamental mode that has a larger extinction ratio in the green highlighted region in Fig. 4(c). The measured resonant wavelengths are plotted as the scatter points in Fig. 4(d). The TDWS is linearly fitted to be 10.96 pm/K, among which the thermorefractive contribution is 7.42 pm/K. The TOC_{eff} of the oxide-substrate waveguide is derived to be 7.28×10^{-6} RIU/K, over 6 times larger than that of the quartz-substrate waveguide in magnitude. The negative and small TOC_{eff} of the quartz-substrate waveguide illustrates that crystal quartz can be used to adjust the waveguide thermo-optic coefficient, which may enable thermorefractive noise engineering. Through proper design of the waveguide geometry, the mode overlap with the quartz substrate can be manipulated, and thus, the TOC_{eff} of the optical modes can be adjusted to be *close-to-zero* and, in turn, the thermorefractive noise of the optical modes will be suppressed as it scales with the square of the TOC_{eff}.[9]

For optical reference cavities, it is desirable to have high Q factors and small thermal noise. In the absence of the cavity's own noise

sources, the rms frequency difference of a locked laser relative to the cavity resonance is inversely proportional to its optical Q factors.[8] Thus, high Q cavities enable tight frequency locking and stabilization. The resonator's loaded Q factor is bounded by its intrinsic Q factor, and the intrinsic Q factor is determined by the waveguide propagation loss α_w, which includes waveguide surface roughness scattering loss, material bulk absorption loss, and waveguide surface absorption loss.[33] Given a high enough Q factor, the stability of the laser frequency is determined by the thermodynamic fluctuations of the cavity resonance that come from thermorefractive and thermal expansion effects. The thermorefractive-related frequency noises are proportional to α_n^2,[9–11] where $\alpha_n = (1/n)(dn/dT)$ is the thermorefractive coefficient. Since this study focuses on lowering the thermo-optic coefficient, we define a figure of merit (FOM) to compare the performance of our Ta_2O_5 on a quartz resonator with other on-chip cavities in different platforms. For fair comparison, we define the FOM given as

$$FOM = \alpha_n^2 \alpha_w, \qquad (3)$$

TABLE I. Comparison of a few integrated photonic waveguides.

Core	Clad	Substrate	α_w (m^{-1})	TOC$_{eff}$ ($\times 10^{-6}$ K^{-1})	α_n ($\times 10^{-6}$ K^{-1})	FOM (K^{-2} m^{-1})[a]	References
Ta$_2$O$_5$	SiO$_2$	Quartz	27.400	−1.14	−0.732	1.47×10^{-11}	This work
Ta$_2$O$_5$	SiO$_2$	SiO$_2$	6.355	7.31	4.79	1.46×10^{-10}	This work
Ta$_2$O$_5$	SiO$_2$	SiO$_2$	55.952	5.75	3.03	5.14×10^{-10}	34
Si$_3$N$_4$	SiO$_2$	SiO$_2$	1.266	24.5	13.4	2.28×10^{-10}	12
Silica	Air	Air	0.034	9.8	6.76	1.58×10^{-12}	8
Si$_3$N$_4$	TiO$_2$	SiO$_2$	9.210	−4.53	−1.25	5.80×10^{-11}	35
Si	Polymer	SiO$_2$	115.128	−2.21	−2.51	1.79×10^{-10}	36

[a]Lower is better.

where α_w is the waveguide propagation loss. This FOM does not take the resonator design into consideration but only compares waveguide propagation loss and thermo-optic properties among different waveguide platforms. A lower FOM is preferred, meaning tighter frequency locking and smaller thermorefractive-related frequency noise when locked. Table I summarizes a few representative designs with respect to this FOM. Our Ta$_2$O$_5$ on the quartz resonator outperforms TiO$_2$- and polymer-based thermo-engineered resonators. It features a lower FOM than Si$_3$N$_4$ on an oxide resonator[12] but not as low as the silica resonator reported in Ref. 8 because the silica resonator has ultra-low loss. To further improve the performance of our Ta$_2$O$_5$ on the quartz resonator, the waveguide loss needs to be reduced, which will be discussed in Sec. V.

V. DISCUSSION AND CONCLUSION

In conclusion, we report fabrication and characterization of the first demonstrated Ta$_2$O$_5$-core/crystal quartz-substrate waveguides. Low waveguide propagation losses are measured to be 1.19 dB/cm at 1550 nm and lower than 1.33 dB/cm across the 1525 nm–1610 nm range using the OFDR method, agreeing well with the loss derived from the Q measurement. The loaded Q factors measured from two different setups correlate reasonably well with slight differences that may come from measurement variations. The thermo-optic coefficient of the waveguide is −1.14 × 10^{-6} RIU/K. The platform can be useful to frequency precision applications such as integrated optical reference cavities and optical frequency combs where the *close-to-zero* waveguide thermorefractive coefficient can help mitigate the thermally induced frequency noise in these cavities.

While the losses in these quartz-substrate waveguides are slightly better than previously reported Ta$_2$O$_5$ waveguides,[37] it may be possible to further reduce propagation loss if material absorption can be mitigated. The main contribution of the propagation loss comes from the material absorption in the core and upper cladding region. The bottom substrate quartz has low material absorption at 1550 nm since quartz-based whispering-gallery-mode resonators can achieve billion Q factors.[18] The Rayleigh scattering loss is expected to be small and should not be the dominant factor because the measured sidewall roughness, 2.76 nm rms (see the supplementary material), is close to the previously demonstrated ultra-low-loss Ta$_2$O$_5$ waveguides,[27] which achieved 3 dB/m performance. Thermal annealing was not applied on the quartz-substrate

devices, thus significant absorption loss can happen due to the presence of SiO–H bonds in SiO$_2$ cladding and oxygen deficiency in the as-grown Ta$_2$O$_5$ films.[37] In fact, the Ta$_2$O$_5$ on the thermal oxide resonator, whose transmission spectrum is shown in Fig. 4(c), was annealed after SiO$_2$ cladding deposition following the same procedure in Ref. 27, and it has a loaded Q factor as high as 0.945 × 10^6 and an intrinsic Q of 1.07 × 10^6. The propagation loss of the oxide-substrate waveguide is 0.276 dB/cm (see the supplementary material), 4.34 times smaller than that of the quartz-substrate waveguide, indicating the significant impact from the annealing process. The material absorption loss from the top cladding can also be possibly mitigated by using deuterated SiO$_2$ in a low-temperature deposition method.[38]

It is worth noting that the TDWS of the quartz-substrate resonator is larger than that of the oxide-substrate device since crystal quartz has a large thermal expansion coefficient (α_o = 13.2 × 10^{-6}/K). With thermorefractive effect suppressed in the quartz-substrate resonator, thermal expansion becomes the dominant effect, as indicated in Fig. 4(b). To create temperature insensitive optical cavities, both the thermal expansion[39] and thermorefractive effects must be controlled. To mitigate the thermal expansion effect, a thinner Ta$_2$O$_5$-core waveguide can be designed in favor of a larger mode overlap with the quartz substrate, yielding a more negative TOC$_{eff}$ to compensate the positive thermal expansion coefficient. The demonstrated device has 500 μm-thick quartz bottom cladding and 6 μm-thick SiO$_2$ upper cladding. Considering that the majority mass of the waveguide is from quartz, it is not surprising that the thermal expansion effect is dominated by the substrate. To further suppress the thermal expansion effect, the quartz layer can be thinned and bonded to an ultra-low-expansion substrate, which will be the subject of future study.

VI. METHODS

Fabrication methods. Fabrication of the waveguide starts with sputtering the amorphous Ta$_2$O$_5$ film on 0.5 mm-thick, 100 mm-diameter single-side polished z-cut optical-grade crystal quartz wafers. The film thickness is measured to be ~125 nm after deposition. The waveguide structures are patterned using a photoresist mask by a 248 nm ASML stepper lithography tool followed by inductively coupled plasma etching. The etching recipe uses CHF$_3$/CF$_4$/O$_2$ gas flow of 25/5/10 SCCM, accompanied by a

pressure of 0.5 Pa, with a RF source power of 500 W and a RF bias power of 50 W. The photoresist is stripped by O_2 ashing followed by the n-methyl-2-pyrrolidone solvent soaking in an ultrasonic heat bath and piranha cleaning. A layer of 6 μm TEOS-PECVD SiO_2 is deposited as the upper cladding on the etched wafer. The wafer then undergoes dicing into several dies for experimental characterization.

Q factor measurement using a RF calibrated MZI setup. An unbalanced fiber-based MZI was used as a reference frequency spectrum to accurately measure the resonator Q.[40] The free spectral range of the MZI is pre-calibrated to be 5.87 MHz. A tunable laser is connected to both the MZI and the device under test (DUT). The laser frequency was swept in time using a microwave synthesizer and the interferometer FSR was measured by monitoring the transmitted power on a synchronized oscilloscope. By simultaneously scanning the laser frequency through both the MZI and the DUT, the MZI fringe spacing provides a radiofrequency calibrated frequency reference for the accurate evaluation of resonator Q factors. The FWHM of the resonator is estimated by fitting the resonator transmission spectrum to a Lorentzian curve. A more detailed discussion and a setup figure can be found in the supplementary material.

Q factor measurement using a direct laser tuning transmission setup. A tunable laser (HP81640A) with a built-in wavelength sweeping functionality is connected to the device under test, and the transmitted power is measured by the power meter (HP81532A). An automation program written in Python controls the laser wavelength with 0.1 pm resolution and synchronizes the power injection and collection process.

Waveguide loss extraction and intrinsic Q factor calculation. The waveguide propagation loss is calculated based on the following equation:[41]

$$Q_{load} = \frac{\pi n_g L \sqrt{ra}}{\lambda_{res}(1 - ra)}, \quad (4)$$

where n_g is the group index of the waveguide and is derived to be 1.7168 from the measured FSR of the resonator shown in Fig. 2(a), $L = 2\pi R$ is the perimeter of the ring resonator and $R = 1.6$ mm is the radius of the ring, λ_{res} is the resonant wavelength, $r = \sqrt{(1 - k^2)}$ is the self-coupling coefficient, where $k^2 = 0.08$ is the measured power coupling coefficient, and a is the single-pass amplitude transmission and is related to the power attenuation coefficient α [1/m] as $a^2 = \exp(-\alpha L)$. With the derived propagation loss, the intrinsic Q of the resonator is estimated by the following equation:[42]

$$Q_{int} = \frac{2\pi n_g}{\alpha \lambda_{res}}. \quad (5)$$

Waveguide loss measurement using OFDR methods. An optical backscatter reflectometer (Luna OBR 4400) injects a pulse that contains a wide spectral range (1525 nm–1610 nm) into the waveguide under test. The reflected signal is collected to map the discontinuities with micrometer-level spatial resolution along the optical path, as shown in the inset of Fig. 3(a). The propagation loss spectrum is obtained by analyzing the backscattered signal in the black region through linear curve fitting at each wavelength, which gives the propagation loss spectrum regardless of the fiber-to-chip coupling loss.

SUPPLEMENTARY MATERIAL

Details of the waveguide sidewall roughness, simulation models and material properties, Ta_2O_5 on oxide substrate waveguide loss and resonator Q factors, and the RF calibrated MZI setup to measure Q factors can be found in the supplementary material.

DATA AVAILABILITY

The data that support the findings of this study are available from the corresponding author upon reasonable request.

REFERENCES

[1]M. G. Boshier, D. Berkeland, E. A. Hinds, and V. Sandoghdar, "External-cavity frequency-stabilization of visible and infrared semiconductor lasers for high resolution spectroscopy," Opt. Commun. **85**, 355–359 (1991).

[2]Y. Bitou, "High-accuracy displacement metrology and control using a dual Fabry-Perot cavity with an optical frequency comb generator," Precis. Eng. **33**, 187–193 (2009).

[3]J. Grotti, S. Koller, S. Vogt, S. Häfner, U. Sterr, C. Lisdat, H. Denker, C. Voigt, L. Timmen, A. Rolland, F. N. Baynes, H. S. Margolis, M. Zampaolo, P. Thoumany, M. Pizzocaro, B. Rauf, F. Bregolin, A. Tampellini, P. Barbieri, M. Zucco, G. A. Costanzo, C. Clivati, F. Levi, and D. Calonico, "Geodesy and metrology with a transportable optical clock," Nat. Phys. **14**, 437–441 (2018).

[4]A. D. Ludlow, M. M. Boyd, J. Ye, E. Peik, and P. O. Schmidt, "Optical atomic clocks," Rev. Mod. Phys. **87**, 637–701 (2015).

[5]M. Schioppo, R. C. Brown, W. F. McGrew, N. Hinkley, R. J. Fasano, K. Beloy, T. H. Yoon, G. Milani, D. Nicolodi, J. A. Sherman, N. B. Phillips, C. W. Oates, and A. D. Ludlow, "Ultrastable optical clock with two cold-atom ensembles," Nat. Photonics **11**, 48–52 (2017).

[6]D. G. Matei, T. Legero, S. Häfner, C. Grebing, R. Weyrich, W. Zhang, L. Sonderhouse, J. M. Robinson, J. Ye, F. Riehle, and U. Sterr, "1.5 μm lasers with sub-10 mHz linewidth," Phys. Rev. Lett. **118**, 263202 (2017).

[7]T. Kessler, C. Hagemann, C. Grebing, T. Legero, U. Sterr, F. Riehle, M. J. Martin, L. Chen, and J. Ye, "A sub-40-mHz-linewidth laser based on a silicon single-crystal optical cavity," Nat. Photonics **6**, 687–692 (2012).

[8]H. Lee, M.-G. Suh, T. Chen, J. Li, S. A. Diddams, and K. J. Vahala, "Spiral resonators for on-chip laser frequency stabilization," Nat. Commun. **4**, 2468 (2013).

[9]M. L. Gorodetsky and I. S. Grudinin, "Fundamental thermal fluctuations in microspheres," J. Opt. Soc. Am. B **21**, 697–705 (2004).

[10]J. Lim, A. A. Savchenkov, E. Dale, W. Liang, D. Eliyahu, V. Ilchenko, A. B. Matsko, L. Maleki, and C. W. Wong, "Chasing the thermodynamical noise limit in whispering-gallery-mode resonators for ultrastable laser frequency stabilization," Nat. Commun. **8**, 8 (2017).

[11]A. Savchenkov and A. Matsko, "Calcium fluoride whispering gallery mode optical resonator with reduced thermal sensitivity," J. Opt. **20**, 035801 (2018).

[12]G. Huang, E. Lucas, J. Liu, A. S. Raja, G. Lihachev, M. L. Gorodetsky, N. J. Engelsen, and T. J. Kippenberg, "Thermorefractive noise in silicon-nitride microresonators," Phys. Rev. A **99**, 061801 (2019).

[13]A. A. Savchenkov, A. B. Matsko, V. S. Ilchenko, N. Yu, and L. Maleki, "Whispering-gallery-mode resonators as frequency references. II. Stabilization," J. Opt. Soc. Am. B **24**, 2988–2997 (2007).

[14]W. Loh, J. Becker, D. C. Cole, A. Coillet, F. N. Baynes, S. B. Papp, and S. A. Diddams, "A microrod-resonator Brillouin laser with 240 Hz absolute linewidth," New J. Phys. **18**, 045001 (2016).

[15]W. Loh, S. Yegnanarayanan, F. O'Donnell, and P. W. Juodawlkis, "Ultra-narrow linewidth Brillouin laser with nanokelvin temperature self-referencing," Optica **6**, 152–159 (2019).

[16]E. S. Magden, M. Y. Peng, J. D. B. Bradley, G. Leake, D. D. Coolbaugh, L. A. Kolodziejski, F. X. Kärtner, and M. R. Watts, "Laser frequency stabilization using pound-drever-hall technique with an integrated TiO$_2$ athermal resonator," in *Conference on Lasers and Electro-Optics (2016)* (Optical Society of America, 2016), p. STu1H.3.

[17]T. Toyoda and M. Yabe, "The temperature dependence of the refractive indices of fused silica and crystal quartz," J. Phys. D: Appl. Phys. **16**, L97–L100 (1983).

[18]V. S. Ilchenko, A. A. Savchenkov, J. Byrd, I. Solomatine, A. B. Matsko, D. Seidel, and L. Maleki, "Crystal quartz optical whispering-gallery resonators," Opt. Lett. **33**, 1569–1571 (2008).

[19]D. V. Strekalov, C. Marquardt, A. B. Matsko, H. G. L. Schwefel, and G. Leuchs, "Nonlinear and quantum optics with whispering gallery resonators," J. Opt. **18**, 123002 (2016).

[20]S. Wang, M. Shah, and J. Crow, "Wave propagation in thin-film optical waveguides using gyrotropic and anisotropic materials as substrates," IEEE J. Quantum Electron. **8**, 212–216 (1972).

[21]Y. Suematsu, Y. Sasaki, K. Furuya, K. Shibata, and S. Ibukuro, "Optical second-harmonic generation due to guided-wave structure consisting of quartz and glass film," IEEE J. Quantum Electron. **10**, 222–229 (1974).

[22]W. K. Burns and A. B. Lee, "Observation of noncritically phase-matched second-harmonic generation in an optical waveguide," Appl. Phys. Lett. **24**, 222–224 (1974).

[23]L.-C. Crasovan, D. Artigas, D. Mihalache, and L. Torner, "Optical Dyakonov surface waves at magnetic interfaces," Opt. Lett. **30**, 3075–3077 (2005).

[24]D. J. Blumenthal, H. Ballani, R. O. Behunin, J. E. Bowers, P. Costa, D. Lenoski, P. A. Morton, S. B. Papp, and P. T. Rakich, "Frequency-stabilized links for coherent WDM fiber interconnects in the Datacenter," J. Lightwave Technol. **38**, 3376–3386 (2020).

[25]D. J. Blumenthal, "Integrated ultra-narrow linewidth stimulated Brillouin scattering (SBS) lasers and their applications," in *Novel In-Plane Semiconductor Lasers XIX* (International Society for Optics and Photonics, 2020), Vol. 11301, p. 1130110.

[26]D. J. Blumenthal, R. Heideman, D. Geuzebroek, A. Leinse, and C. Roeloffzen, "Silicon nitride in silicon photonics," Proc. IEEE **106**, 2209–2231 (2018).

[27]M. Belt, M. L. Davenport, J. E. Bowers, and D. J. Blumenthal, "Ultra-low-loss Ta$_2$O$_5$-core/SiO$_2$-clad planar waveguides on Si substrates," Optica **4**, 532–536 (2017).

[28]Quartz Crystal (SiO$_2$) Optical Material, https://www.crystran.co.uk/optical-materials/quartz-crystal-SiO2.

[29]E. Çetinörgü, B. Baloukas, O. Zabeida, J. E. Klemberg-Sapieha, and L. Martinu, "Mechanical and thermoelastic characteristics of optical thin films deposited by dual ion beam sputtering," Appl. Opt. **48**, 4536–4544 (2009).

[30]B. El-Kareh and L. N. Hutter, *Fundamentals of Semiconductor Processing Technology* (Springer Science & Business Media, 2012).

[31]A. K. Ramdas, "The thermo-optic behaviour of quartz," Proc. Indian Acad. Sci., Ser. A **35**, 89 (1952).

[32]A. W. Elshaari, I. E. Zadeh, K. D. Jöns, and V. Zwiller, "Thermo-optic characterization of silicon nitride resonators for cryogenic photonic circuits," IEEE Photonics J. **8**, 1–9 (2016).

[33]M. W. Puckett, K. Liu, N. Chauhan, Q. Zhao, N. Jin, H. Cheng, J. Wu, R. O. Behunin, P. T. Rakich, K. D. Nelson, and D. J. Blumenthal, "422 million Q planar integrated all-waveguide resonator with a 3.4 billion absorption limited Q and sub-MHz linewidth," arXiv:2009.07428 [physics] (2020).

[34]C.-L. Wu, Y.-J. Hung, R. Fan, D.-H. Ou, J.-Y. Huang, T.-H. Yen, Y.-J. Chiu, M.-H. Shih, Y.-Y. Lin, A.-K. Chu, and C.-K. Lee, "Tantalum pentoxide (Ta$_2$O$_5$) based athermal micro-ring resonator," OSA Continuum **2**, 1198–1206 (2019).

[35]F. Qiu, A. M. Spring, and S. Yokoyama, "Athermal and high-Q hybrid TiO$_2$–Si$_3$N$_4$ ring resonator via an etching-free fabrication technique," ACS Photonics **2**, 405–409 (2015).

[36]F. Qiu, A. M. Spring, H. Miura, D. Maeda, M.-a. Ozawa, K. Odoi, and S. Yokoyama, "Athermal hybrid silicon/polymer ring resonator electro-optic modulator," ACS Photonics **3**, 780–783 (2016).

[37]C.-L. Wu, B.-T. Chen, Y.-Y. Lin, W.-C. Tien, G.-R. Lin, Y.-J. Chiu, Y.-J. Hung, A.-K. Chu, and C.-K. Lee, "Low-loss and high-Q Ta$_2$O$_5$ based micro-ring resonator with inverse taper structure," Opt. Express **23**, 26268–26275 (2015).

[38]W. Jin, D. D. John, J. F. Bauters, T. Bosch, B. J. Thibeault, and J. E. Bowers, "Deuterated silicon dioxide for heterogeneous integration of ultra-low-loss waveguides," Opt. Lett. **45**, 3340–3343 (2020).

[39]V. B. Braginsky, M. L. Gorodetsky, and S. P. Vyatchanin, "Thermodynamical fluctuations and photo-thermal shot noise in gravitational wave antennae," Phys. Lett. A **264**, 1–10 (1999).

[40]J. Li, H. Lee, K. Y. Yang, and K. J. Vahala, "Sideband spectroscopy and dispersion measurement in microcavities," Opt. Express **20**, 26337–26344 (2012).

[41]W. Bogaerts, P. D. Heyn, T. V. Vaerenbergh, K. D. Vos, S. K. Selvaraja, T. Claes, P. Dumon, P. Bienstman, D. V. Thourhout, and R. Baets, "Silicon microring resonators," Laser Photonics Rev. **6**, 47–73 (2012).

[42]L. Chrostowski and M. Hochberg, *Silicon Photonics Design* (Cambridge University Press, 2015).